Frontiers of Information Technology & Electronic Engineering
www.jzus.zju.edu.cn; engineering.cae.cn; www.springerlink.com
ISSN 2095-9184 (print); ISSN 2095-9230 (online)
E-mail: jzus@zju.edu.cn

Enhanced solution to the surface–volume–surface EFIE for arbitrary metal–dielectric composite objects*

Han WANG, Mingjie PANG, Hai LIN‡

State Key Laboratory of CAD & CG, Zhejiang University, Hangzhou 310027, China

E-mail: wanghanaviva@zju.edu.cn; mjpang@zju.edu.cn; lin@cad.zju.edu.cn

Received Aug. 10, 2021; Revision accepted Nov. 24, 2021; Crosschecked Apr. 13, 2022; Published online June 7, 2022

Abstract: The surface–volume–surface electric field integral equation (SVS-EFIE) can lead to complex equations, laborious implementation, and unacceptable computational complexity in the method of moments (MoM). Therefore, a general matrix equation (GME) is proposed for electromagnetic scattering from arbitrary metal–dielectric composite objects, and its enhanced solution is presented in this paper. In previous works, MoM solution formulation of SVS-EFIE considering only three-region metal–dielectric composite scatters was presented, and the two-stage process resulted in two integral operators in SVS-EFIE, which is arduous to implement and is incapable of reducing computational complexity. To address these difficulties, GME, which is versatile for homogeneous objects and composite objects consisting of more than three sub-regions, is proposed for the first time. Accelerated solving policies are proposed for GME based on coupling degree concerning the spacing between sub-regions, and the coupling degree standard can be adaptively set to balance the accuracy and efficiency. In this paper, the reformed addition theorem is applied for the strong coupling case, and the iterative method is presented for the weak coupling case. Parallelism can be easily applied in the enhanced solution. Numerical results demonstrate that the proposed method requires only 11.6% memory and 11.8% CPU time on average compared to the previous direct solution.

Key words: Composite object; Integral equation; Method of moments (MoM); Addition theorem; Iterative method

https://doi.org/10.1631/FITEE.2100387 **CLC number:** TP391

1 Introduction

The electromagnetic (EM) simulation of metal–dielectric composite structures plays an essential role in many areas of electromagnetism such as planar microstrips, radome analysis, remote sensing, and radar applications (Lu and Chew, 2000; Lu, 2003; Xie and Li, 2018). In previous works (Poggio and Miller, 1973; Rao et al., 1982; Ergul and Gurel, 2009), one unknown was enough for a metal object, whereas two unknowns were required to reproduce the sought field throughout a dielectric object in the surface integral equation (SIE).

Recently, the surface–volume–surface electric field integral equation (SVS-EFIE) (Menshov and Okhmatovski, 2013; Lori et al., 2018) has been proposed for scattering analysis of two-dimensional (2D) and three-dimensional (3D) dielectric bodies. Furthermore, SVS-EFIE has been applied to dielectric objects in multilayered media (Zheng et al., 2018) and metal–dielectric composite objects (Gholami and Okhmatovski, 2020). The analytic solution to SVS-EFIE has also been presented for homogeneous dielectric spheres, which validates the rigorous nature of SVS-EFIE (Goni and Okhmatovski, 2021). SVS-EFIE requires only a single unknown on the boundary of the dielectric body to determine the sought field with a two-stage process (Lori et al.,

‡ Corresponding author

* Project supported by the National Key Research and Development Program, China (No. 2020YFC2201302)

ORCID: Han WANG, https://orcid.org/0000-0002-9348-5806; Hai LIN, https://orcid.org/0000-0002-1682-8465

2018). In the first stage, the unknown currents on the boundary of the scatterer were used to obtain the total field distribution throughout the volume of the scatterer. The entire field outside the scatterer was obtained in the second stage by the total field distribution throughout the volume using the volume equivalence principle. However, the two-stage process will generate two additional dense matrices in the method of moments (MoM). Considering a metal–dielectric composite object discretized by tetrahedrons, $N_{\rm v}$ tetrahedrons in its volume and $N_{\rm s}$ triangle pairs on its boundary were observed, where $N_{\rm v}=N_{\rm s}^{\alpha}$ and $\alpha\in(1,1.5)$ (Gholami et al., 2019). In solving SVS-EFIE using MoM with the RWG basis function (Rao et al., 1982) and Galerkin method, $N_{\rm s}$ unknown coefficients must be determined. Apart from the normal $N_{\rm s}\times N_{\rm s}$ dense matrix, the first-stage process leads to an additional $N_{\rm s}\times N_{\rm v}$ dense matrix, and the second-stage process leads to an additional $N_{\rm v}\times N_{\rm s}$ dense matrix. The hierarchical ($\mathcal{H}$-) matrix has been introduced for fast analysis of SVS-EFIE (Gholami et al., 2019). The general mathematical framework of the $\mathcal{H}$-matrix provides a highly compact representation of the impedance matrix, which can reduce the time and memory usage for solving SVS-EFIE. However, the $\mathcal{H}$-matrix accelerated method does not consider the difference between the strong coupling and weak coupling cases among the composite objects. Moreover, although SVS-EFIE has been applied to metal–dielectric composite objects in Gholami and Okhmatovski (2020), only the MoM solution formulation considering three-region metal–dielectric composite scatterers has been presented. Therefore, although SVS-EFIE can efficiently reduce the number of unknowns in SIE for dielectric scatterers, solving SVS-EFIE using MoM will result in complex equations, laborious implementation, and unacceptable computational complexity.

To address these problems, an enhanced solution to SVS-EFIE for arbitrary metal–dielectric composite objects is proposed in this study. MoM is the core solver of the enhanced solution. In addition, CPU parallelism (Dagum and Menon, 1998; Hariharan et al., 2002) can be easily applied to improve the computational efficiency of the accelerated methods. Two main contributions of this paper are as follows:

1. A general matrix equation (GME) is presented to solve SVS-EFIE for arbitrary metal–dielectric composite objects using MoM. The new GME is highly adaptive to homogeneous objects and composite objects that consist of more than three sub-regions. Furthermore, GME has a simple form that is easy to implement on computers.

2. An enhanced solution to GME is presented. Two acceleration policies are proposed for solving GME based on coupling degree, which can be set adaptively to balance the accuracy and efficiency. For the strong coupling case, the addition theorem, which has been widely used in computational electromagnetics, is adopted to accelerate matrix–vector multiplication (MVM) and matrix–matrix multiplication (Song J et al., 1997; Chew et al., 2001). For the weak coupling case, the iterative method is adopted to consider the weak coupling among different parts, and adaptive cross approximation (ACA) (Zhao et al., 2005) is introduced to compress the coupling matrix among different sub-regions. In the enhanced solution, computational complexity is reduced to $O(N_{\rm s}^{\alpha}\log N_{\rm s})$, where $N_{\rm s}$ is the number of total triangle pairs on the boundary of the composite objects.

2 Basic principle of SVS-EFIE

Consider the scattering of the time-harmonic incident field $\boldsymbol{E}^{\rm inc}$ on a homogeneous dielectric object of volume V. Using the volume equivalence principle, the electric field inside and outside the scatterer can be defined as

$$\boldsymbol{E}(\boldsymbol{r})=\boldsymbol{E}^{\rm inc}(\boldsymbol{r})+k_0^2(\epsilon-1)\int_V\overline{\overline{G}}_{\rm e0}(\boldsymbol{r},\boldsymbol{r}')\boldsymbol{E}(\boldsymbol{r}'){\rm d}v', \tag{1}$$

where $\boldsymbol{r}$ is the observation point in the space, $\boldsymbol{r}'$ is the source point inside the scatterer, ϵ is the complex relative permittivity, $k_0=\omega\sqrt{\epsilon_0\mu_0}$ is the wavenumber of vacuum, and ϵ_0 and μ_0 are the permittivity and permeability of vacuum, respectively. The 3D dyadic Green function of free space is

$$\overline{\overline{G}}_{\rm e0}(\boldsymbol{r},\boldsymbol{r}')=\left(\frac{\nabla\nabla}{k_0^2}+\overline{\overline{I}}\right)\frac{{\rm e}^{-{\rm i}k_0|\boldsymbol{r}-\boldsymbol{r}'|}}{4\pi|\boldsymbol{r}-\boldsymbol{r}'|}, \tag{2}$$

where $\overline{\overline{I}}$ is the idem-factor.

By the homogeneous wave equation, the total electric field inside the scatterer V satisfies

$$\nabla\times\nabla\times\boldsymbol{E}(\boldsymbol{r})-k_\epsilon^2\boldsymbol{E}(\boldsymbol{r})=0,\quad \boldsymbol{r}\in V\backslash\partial V, \tag{3}$$

where $k_\epsilon=k_0\sqrt{\epsilon}$ is the wavenumber inside the homogeneous non-magnetic medium.

It can be written as a superposition of spherical waves emanating from object boundary ∂V as

$$\boldsymbol{E}(\boldsymbol{r}) = -\mathrm{i}\omega\mu_0 \int_{\partial V} \overline{\overline{G}}_{\mathrm{e}\epsilon}(\boldsymbol{r},\boldsymbol{r}')\boldsymbol{J}(\boldsymbol{r}')\mathrm{d}s', \boldsymbol{r} \in V\backslash\partial V. \tag{4}$$

The 3D dyadic Green function is

$$\overline{\overline{G}}_{\mathrm{e}\epsilon}(\boldsymbol{r},\boldsymbol{r}') = \left(\frac{\nabla\nabla}{k_\epsilon^2} + \overline{\overline{I}}\right)\frac{\mathrm{e}^{-\mathrm{i}k_\epsilon|\boldsymbol{r}-\boldsymbol{r}'|}}{4\pi|\boldsymbol{r}-\boldsymbol{r}'|}. \tag{5}$$

Substituting Eq. (4) into Eq. (1) and restricting the observation domain to the surface of the scatterer yields SVS-EFIE as (Lori et al., 2018)

$$\begin{aligned}&\hat{\boldsymbol{t}}\boldsymbol{E}^{\mathrm{inc}}(\boldsymbol{r})\\ =&\mathrm{i}\omega\mu_0\hat{\boldsymbol{t}}\left(-\int_{\partial V}\overline{\overline{G}}_{\mathrm{e}\epsilon}(\boldsymbol{r},\boldsymbol{r}'')\boldsymbol{J}(\boldsymbol{r}'')\mathrm{d}s'' + k_0^2(\epsilon-1)\right.\\ &\left.\cdot\int_V \overline{\overline{G}}_{\mathrm{e}0}(\boldsymbol{r},\boldsymbol{r}')\oint_{\partial V}\overline{\overline{G}}_{\mathrm{e}\epsilon}(\boldsymbol{r}',\boldsymbol{r}'')\boldsymbol{J}(\boldsymbol{r}'')\mathrm{d}s''\mathrm{d}v'\right),\ \boldsymbol{r}\in\partial V,\end{aligned} \tag{6}$$

where $\hat{\boldsymbol{t}}$ is the tangential vector to the surface ∂V.

3 GME of SVS-EFIE for composite objects

SVS-EFIE was extended to SVS-surface-EFIE (SVS-S-EFIE) for composite conductor–dielectric materials by Gholami and Okhmatovski (2020), but only the MoM solution formulation for three-region composite objects was presented. Here, we present a general solution form to SVS-EFIE based on the MoM for arbitrary metal–dielectric composite objects. Homogeneous objects and composite objects consisting of more than three sub-regions can be easily expanded from GME.

Consider an arbitrary metal–dielectric composite object that consists of P_{c} conductor regions and P_{d} dielectric regions. The index range of the metal regions is from 1 to P_{c}, and the index range of dielectric regions is from $P_{\mathrm{c}}+1$ to $P_{\mathrm{c}}+P_{\mathrm{d}}$. By the equivalence principle and enforcement of the vanishing tangential electric field on the surface of the metal region, the sum of the tangential part of the incident field and the total scattered field generated from all sub-regions of the composite objects on the metal region surface equals zero. By the volume–surface equivalence principle (Lu and Chew, 2000; Xie and Li, 2018) and restricting the observation point to the boundary of the dielectric region, the tangential part of the total field of the dielectric region's boundary is equal to the sum of the incident field of the region and scattered field generated from all the sub-regions of the composite objects. Adjusting these pieces of information, the extended SVS-EFIE for composite objects is represented as

$$\hat{\boldsymbol{t}}_p\boldsymbol{E}_p^{\mathrm{inc}}(\boldsymbol{r}_p) = \begin{cases} -\hat{\boldsymbol{t}}_p\sum\limits_{q=1}^{P_{\mathrm{c}}+P_{\mathrm{d}}}\boldsymbol{E}_q^{\mathrm{sca}}(\boldsymbol{r}_p),\\ \quad \boldsymbol{r}_p\in\partial V_p, p\in[1,P_{\mathrm{c}}],\\ \hat{\boldsymbol{t}}_p\left(\boldsymbol{E}_p(\boldsymbol{r}_p) - \sum\limits_{q=1}^{P_{\mathrm{c}}+P_{\mathrm{d}}}\boldsymbol{E}_q^{\mathrm{sca}}(\boldsymbol{r}_p)\right),\\ \quad \boldsymbol{r}_p\in\partial V_p, p\in[P_{\mathrm{c}}+1,P_{\mathrm{c}}+P_{\mathrm{d}}],\end{cases} \tag{7}$$

where $\boldsymbol{E}_p^{\mathrm{inc}}$ is the incident field of region p, $\boldsymbol{E}_q^{\mathrm{sca}}$ is the scattering field generated by region q, $\boldsymbol{E}_p$ is the total field of the dielectric region p, $\boldsymbol{r}_p$ is the observation point on the boundary of region p, $\hat{\boldsymbol{t}}_p$ is the tangential vector to the boundary of region p, and ∂V_p is the boundary of region p. Moreover, using Eq. (4), the total field of the dielectric region p is represented as

$$\begin{aligned}&\boldsymbol{E}_p(\boldsymbol{r}_p) = -\mathrm{i}\omega\mu_0\int_{\partial V_p}\overline{\overline{G}}_{\mathrm{e}\epsilon_p}(\boldsymbol{r},\boldsymbol{r}')\boldsymbol{J}_p(\boldsymbol{r}')\mathrm{d}s',\\ &\boldsymbol{r}\in V_p\backslash\partial V_p,\ \boldsymbol{r}_p\in\partial V_p,\ p\in[P_{\mathrm{c}}+1,P_{\mathrm{c}}+P_{\mathrm{d}}],\end{aligned} \tag{8}$$

where $\boldsymbol{J}_p$ is the unknown equivalent current on the boundary of region p. The Green function of the dielectric region p is

$$\overline{\overline{G}}_{\mathrm{e}\epsilon_p}(\boldsymbol{r},\boldsymbol{r}') = \left(\frac{\nabla\nabla}{k_{\epsilon_p}^2} + \overline{\overline{I}}\right)\frac{\mathrm{e}^{-\mathrm{i}k_{\epsilon_p}|\boldsymbol{r}-\boldsymbol{r}'|}}{4\pi|\boldsymbol{r}-\boldsymbol{r}'|}. \tag{9}$$

By the surface equivalence principle and Eq. (6), the scattered field from different sub-regions is represented in Eq. (10) at the top of the next page. In Eq. (10), $\boldsymbol{J}_q$ is the unknown equivalent current on the boundary of region q, ∂V_q is the boundary of the metal region q, V_q is the volume of the dielectric part q, and ϵ_q is the complex relative permittivity of the dielectric region q.

Combining Eqs. (7) and (8), the general form of the SVS-EFIE for composite conductor–dielectric materials is produced in Eq. (10). In solving equations using MoM, the surfaces of metal regions are discretized by triangles, and the volumes of dielectric regions are discretized by tetrahedrons. The

$$\boldsymbol{E}_q^{\mathrm{sca}}(\boldsymbol{r})=\begin{cases}-\mathrm{i}\omega\mu_0\oint\limits_{\partial V_q}\overline{\overline{G}}_{\mathrm{e}0}(\boldsymbol{r},\boldsymbol{r}_q')\boldsymbol{J}_q(\boldsymbol{r}_q')\mathrm{d}s',\boldsymbol{r}_q'\in\partial V_q,\ q\in[1,P_{\mathrm{c}}],\\ -\mathrm{i}\omega\mu_0k_0^2(\epsilon-1)\int\limits_{V_q}\overline{\overline{G}}_{\mathrm{e}0}(\boldsymbol{r},\boldsymbol{r}_q')\oint\limits_{\partial V_q}\overline{\overline{G}}_{\mathrm{e}\epsilon_q}(\boldsymbol{r}_q',\boldsymbol{r}_q'')\boldsymbol{J}_q(\boldsymbol{r}_q'')\mathrm{d}s''\mathrm{d}v',\boldsymbol{r}_q'\in V_q,\boldsymbol{r}_q''\in\partial V_q,q\in[P_{\mathrm{c}}+1,P_{\mathrm{c}}+P_{\mathrm{d}}].\end{cases}\tag{10}$$

unknown currents $\boldsymbol{J}_q$ defined on the boundary ∂V_q of region q can be performed using the RWG basis function (Rao et al., 1982), which is defined as

$$\boldsymbol{f}_n(\boldsymbol{r})=\begin{cases}\dfrac{\boldsymbol{r}-\boldsymbol{v}_n^+}{2A_n^+},\ \boldsymbol{r}\in S_n^+,\\ \dfrac{\boldsymbol{v}_n^--\boldsymbol{r}}{2A_n^-},\ \boldsymbol{r}\in S_n^-,\end{cases}\tag{11}$$

where $\boldsymbol{v}_n^{\pm}$ is the vertex that is opposite to the interior edge and $A_n^{\pm}$ is the area of triangle $S_n^{\pm}$ as illustrated in Fig. 1.

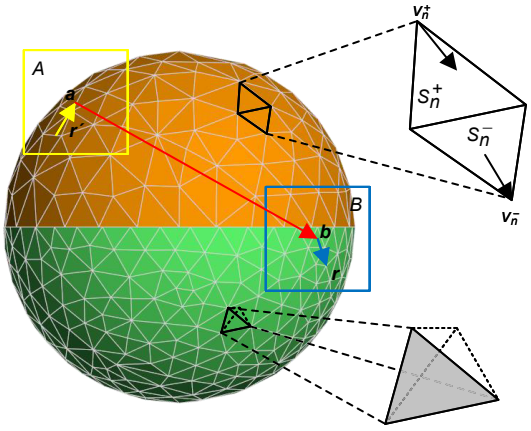

Fig. 1 Illustration of the mesh, basis functions, and wave translation

(1) Mesh: The metal region of the model, colored in orange, is discretized by triangle pairs, and the dielectric region of the model, colored in green, is discretized by tetrahedrons. (2) Basis functions: The RWG basis function represents the equivalent currents on the boundary of each region. The RWG basis function is defined on the triangle pairs. (3) Wave translation: For clarity, a square represents a group (cube). Groups A and B in the same layer are marked as relatively far groups for each other. $\boldsymbol{a}$ and $\boldsymbol{b}$ are geometric centers of these two groups, $\boldsymbol{r}'$ is the source point, and $\boldsymbol{r}$ is the observation point. The yellow arrow represents the upward aggregation, the red arrow represents the translation, and the blue arrow represents the downward disaggregation. Fields in group A are first aggregated to point $\boldsymbol{a}$. Then the field at point $\boldsymbol{a}$ is translated to all the relatively far groups of group A. All received fields at point $\boldsymbol{b}$ are finally disaggregated to child cubes or basis functions in group B. References to color refer to the online version of this figure

Using the Galerkin method, the GME can be written as

$$\boldsymbol{V}^p=\begin{cases}\sum\limits_{q=1}^{P_{\mathrm{c}}}\boldsymbol{Z}_{\mathrm{SS}}^{pq}\boldsymbol{I}^q-\sum\limits_{q=P_{\mathrm{c}}+1}^{P_{\mathrm{c}}+P_{\mathrm{d}}}\boldsymbol{Z}_{\mathrm{SVS}}^{pq}\boldsymbol{I}^q,\ p\in[1,P_{\mathrm{c}}],\\ \boldsymbol{Z}_{\mathrm{SS}}^{p}\boldsymbol{I}^p-\sum\limits_{q=1}^{P_{\mathrm{c}}}\boldsymbol{Z}_{\mathrm{SS}}^{pq}\boldsymbol{I}^q-\sum\limits_{q=P_{\mathrm{c}}+1}^{P_{\mathrm{c}}+P_{\mathrm{d}}}\boldsymbol{Z}_{\mathrm{SVS}}^{pq}\boldsymbol{I}^q,\\ \qquad p\in[P_{\mathrm{c}}+1,P_{\mathrm{c}}+P_{\mathrm{d}}],\end{cases}\tag{12}$$

where $\boldsymbol{V}^p$ is the excitation matrix related to the left part in Eq. (7). $\boldsymbol{I}^p$ and $\boldsymbol{I}^q$ are the unknown surface current coefficients of regions p and q, respectively. The dielectric surface-to-surface integral matrix $\boldsymbol{Z}_{\mathrm{SS}}^p$ is generated from Eq. (8), and the matrix elements are computed by

$$\begin{aligned}&[\boldsymbol{Z}_{\mathrm{SS}}^p]_{m,n}\\&=-\mathrm{i}\omega\mu_0\int\limits_{\boldsymbol{f}_m}\boldsymbol{f}_m(\boldsymbol{r})\int\limits_{\boldsymbol{f}_n}\overline{\overline{G}}_{\mathrm{e}\epsilon_p}(\boldsymbol{r},\boldsymbol{r}')\boldsymbol{f}_n(\boldsymbol{r}')\mathrm{d}\boldsymbol{r}'\mathrm{d}\boldsymbol{r},\\&\boldsymbol{f}_n\in\partial V_p,\ \boldsymbol{f}_m\in\partial V_p,\ p\in[P_{\mathrm{c}}+1,P_{\mathrm{c}}+P_{\mathrm{d}}],\end{aligned}\tag{13}$$

where $\boldsymbol{f}_m$ is the RWG test function and $\boldsymbol{f}_n$ is the RWG basis function.

The metal surface-to-surface integral matrix $\boldsymbol{Z}_{\mathrm{SS}}^{pq}$ is related to the surface-to-surface integral Eq. (10) from conductor part p to part q, and the matrix elements are calculated by

$$\begin{aligned}&[\boldsymbol{Z}_{\mathrm{SS}}^{pq}]_{m,n}\\&=-\mathrm{i}\omega\mu_0\int\limits_{\boldsymbol{f}_m}\boldsymbol{f}_m(\boldsymbol{r})\int\limits_{\boldsymbol{f}_n}\overline{\overline{G}}_{\mathrm{e}0}(\boldsymbol{r},\boldsymbol{r}')\boldsymbol{f}_n(\boldsymbol{r}')\mathrm{d}\boldsymbol{r}'\mathrm{d}\boldsymbol{r},\\&\boldsymbol{f}_n\in\partial V_q,\ \boldsymbol{f}_m\in\partial V_p,\ q\in[1,P_{\mathrm{c}}].\end{aligned}\tag{14}$$

The dielectric SVS integral matrix $\boldsymbol{Z}_{\mathrm{SVS}}^{pq}$ is related to the SVS integral Eq. (10) from dielectric part p to part q, and the matrix elements are

computed by

$$\begin{aligned}&[\boldsymbol{Z}_{\mathrm{SVS}}^{pq}]_{m,n}\\&=-\mathrm{i}\omega\mu_0 k_0^2(\epsilon-1)\int\limits_{\boldsymbol{f}_m}\boldsymbol{f}_m(\boldsymbol{r})\int\limits_{V_q}\overline{\overline{G}}_{\mathrm{e}0}(\boldsymbol{r},\boldsymbol{r}_q')\\&\cdot\oint\limits_{\boldsymbol{f}_n}\overline{\overline{G}}_{\mathrm{e}\epsilon_q}(\boldsymbol{r}_q',\boldsymbol{r}_q'')\boldsymbol{f}_n(\boldsymbol{r}_q'')\mathrm{d}\boldsymbol{r}'\mathrm{d}v',\\&\boldsymbol{f}_n\in\partial V_q,\ \boldsymbol{f}_m\in\partial V_p, q\in[P_{\mathrm{c}}+1,\ P_{\mathrm{c}}+P_{\mathrm{d}}].\end{aligned}\tag{15}$$

The excitation matrix is calculated by

$$[\boldsymbol{V}^p]_m=\int\limits_{\boldsymbol{f}_m}\boldsymbol{E}^{\mathrm{inc}}(\boldsymbol{r})\boldsymbol{f}_m(\boldsymbol{r})\mathrm{d}\boldsymbol{r},\ \boldsymbol{f}_m\in\partial V_p.\tag{16}$$

To handle the three integral operators in Eq. (15), we hypothesize that the total field varies slowly enough to be approximated within each tetrahedron by their values at the centroid of the tetrahedron. Thus, the $N_{\mathrm{s}}^p\times N_{\mathrm{s}}^q$ matrix $\boldsymbol{Z}_{\mathrm{SVS}}^{pq}$ can be written as the multiplication of an $N_{\mathrm{s}}^p\times N_{\mathrm{v}}^q$ matrix $\boldsymbol{Z}_{\mathrm{SV}}$ and an $N_{\mathrm{v}}^q\times N_{\mathrm{s}}^q$ matrix $\boldsymbol{Z}_{\mathrm{VS}}$, where

$$\begin{aligned}&[\boldsymbol{Z}_{\mathrm{SV}}]_{m,n_{\mathrm{t}}}\\&=k_0^2(\epsilon-1)\int\limits_{\boldsymbol{f}_m}\boldsymbol{f}_m(\boldsymbol{r})\int\limits_{V_q^{n_{\mathrm{t}}}}\overline{\overline{G}}_{\mathrm{e}0}(\boldsymbol{r},\boldsymbol{r}')\\&\cdot\left[g_{n_{\mathrm{t}}}^x(\boldsymbol{r}')\ \ g_{n_{\mathrm{t}}}^y(\boldsymbol{r}')\ \ g_{n_{\mathrm{t}}}^z(\boldsymbol{r}')\right]^{\mathrm{T}}\mathrm{d}v\mathrm{d}\boldsymbol{r}',\\&\boldsymbol{f}_m\in\partial V_p,\ V_q^{n_{\mathrm{t}}}\in V_q,\end{aligned}\tag{17}$$

$$\begin{aligned}&[\boldsymbol{Z}_{\mathrm{VS}}^{x,y,z}]_{n_{\mathrm{t}},n}\\&=\left(-\mathrm{i}\omega\mu_0\int\limits_{\boldsymbol{f}_n}\overline{\overline{G}}_{\mathrm{e}\epsilon_q}(\boldsymbol{r}',\boldsymbol{r}'')\boldsymbol{f}_n(r'')\mathrm{d}\boldsymbol{r}''\right)_{x,y,z},\end{aligned}\tag{18}$$

and $\boldsymbol{r}'$ is the centroid of $V_q^{n_{\mathrm{t}}}$.

Note that the integral in Eq. (18) results in a vector, and the x, y, and z components are stored in $\boldsymbol{Z}_{\mathrm{VS}}^x$, $\boldsymbol{Z}_{\mathrm{VS}}^y$, and $\boldsymbol{Z}_{\mathrm{VS}}^z$, respectively. $g_{n_{\mathrm{t}}}^{x,y,z}(\boldsymbol{r})$ is the volume pulse function defined on the tetrahedron element $V^{n_{\mathrm{t}}}$:

$$g_{n_{\mathrm{t}}}^{x,y,z}(\boldsymbol{r})=\begin{cases}1,\ \boldsymbol{r}\in V^{n_{\mathrm{t}}},\\0,\ \boldsymbol{r}\notin V^{n_{\mathrm{t}}}.\end{cases}\tag{19}$$

4 Enhanced solution to GME

The GME of SVS-EFIE can be solved directly, but the computational complexity of the direct solution is unacceptable in practical applications. The dielectric and metal surface-to-surface integral matrices in Eq. (12) require $O(N_{\mathrm{s}}^2)$ memory storage. In addition, these two dense matrices in Eqs. (17) and (18) require $O(N_{\mathrm{s}}N_{\mathrm{v}})$ memory storage. The SVS integral matrix is generated by the multiplication of two dense matrices, leading to time complexity of $O(N_{\mathrm{s}}^2N_{\mathrm{v}})$. In addition, the direct matrix equation solver for GME requires $O(N_{\mathrm{s}}^3)$ CPU time. Therefore, given that $N_{\mathrm{v}}=N_{\mathrm{s}}^{\alpha}$ and $\alpha\in(1,1.5)$, the direct solution to GME has $O(N_{\mathrm{s}}^{1+\alpha})$ space complexity and $O(N_{\mathrm{s}}^{2+\alpha})$ time complexity.

In this study, an enhanced solution of the general form is presented to reduce the computational complexity. Two policies are presented based on the coupling degree concerning the spacing between different sub-regions. For the strong coupling case, the coupling matrices between two sub-regions contribute significantly to the final result. Thus, the coupling matrices should be stored explicitly, and the physical considerations such as the addition theorem are suitable for reducing the computational complexity. For the weak coupling case, the coupling matrices between two sub-regions have a weak influence on the final result. Thus, the coupling matrices can be compressed by an algebraic method such as ACA, and the iterative method is suitable for considering weak coupling.

4.1 Enhanced solution in the strong coupling case

In this study, the method based on the addition theorem is proposed to solve the scattering problems for the composite objects in the strong coupling case. Applying the addition algorithm to the Green function in Eqs. (2) and (9) yields

$$\begin{aligned}&\overline{\overline{G}}_{\mathrm{e}0,\mathrm{e}\epsilon_q}(\boldsymbol{r},\boldsymbol{r}')=\left(\overline{\overline{I}}-\frac{\nabla\nabla'}{k_{0,\epsilon_q}^2}\right)\frac{\mathrm{e}^{-\mathrm{i}k_{0,\epsilon_q}|\boldsymbol{r}-\boldsymbol{r}'|}}{4\pi|\boldsymbol{r}-\boldsymbol{r}'|}\\&=\frac{1}{4\pi}\int\left(\overline{\overline{I}}-\hat{\boldsymbol{k}}\hat{\boldsymbol{k}}\right)\mathrm{e}^{-\mathrm{i}k_{0,\epsilon_q}\hat{\boldsymbol{k}}(\boldsymbol{r}_{\boldsymbol{rb}}-\boldsymbol{r}_{\boldsymbol{r}'\boldsymbol{a}})}\\&\cdot T_L(k_{0,\epsilon_q},\hat{\boldsymbol{k}},\boldsymbol{r}_{\boldsymbol{ba}})\mathrm{d}^2\hat{\boldsymbol{k}},\ |\boldsymbol{r}_{\boldsymbol{ba}}|<|\boldsymbol{r}_{\boldsymbol{rb}}|+|\boldsymbol{r}_{\boldsymbol{r}'\boldsymbol{a}}|,\end{aligned}\tag{20}$$

$$\begin{aligned}&T_L(k_{0,\epsilon_q},\hat{\boldsymbol{k}},\boldsymbol{r}_{\boldsymbol{ba}})\\&=\frac{k}{4\pi}\sum_{l=0}^{L}(-\mathrm{i})^{l+1}(2l+1)h_l^{(2)}(k_{0,\epsilon_q}|\boldsymbol{r}_{\boldsymbol{ba}}|)P_l(\hat{\boldsymbol{k}}\hat{\boldsymbol{r}}_{\boldsymbol{ba}}),\end{aligned}\tag{21}$$

$$\begin{aligned}\boldsymbol{r}-\boldsymbol{r}'&=(\boldsymbol{r}-\boldsymbol{b})+(\boldsymbol{b}-\boldsymbol{a})-(\boldsymbol{r}'-\boldsymbol{a})\\&=\boldsymbol{r}_{\boldsymbol{rb}}+\boldsymbol{r}_{\boldsymbol{ba}}-\boldsymbol{r}_{\boldsymbol{r}'\boldsymbol{a}},\end{aligned}\tag{22}$$

where $\hat{\boldsymbol{k}}$ is the unit direction (radial) vector on the unit sphere, $\boldsymbol{r}'$ is the source point, $\boldsymbol{r}$ is the observation point as illustrated in Fig. 1, and $\boldsymbol{a}$, $\boldsymbol{b}$ are vectors obtained by adding a small offset to $\boldsymbol{r}'$ and $\boldsymbol{r}$, respectively. $P_l(\cdot)$ is a Legendre polynomial of order l, $h_l^{(2)}(\cdot)$ is a spherical Hankel function of the second kind, and L is the truncation order.

Applying the addition theorem to the four matrix elements shown in Section 3 produces new formulas to calculate the elements that satisfy the constraint in Eq. (20).

1. Applying the addition theorem to Eq. (13), the $\boldsymbol{Z}_{\mathrm{SS}}^{p}$ element can be written as

$$\begin{aligned}&[\boldsymbol{Z}_{\mathrm{SS}}^{p}]_{m,n}\\&=-\frac{\mathrm{i}\omega\mu_0}{4\pi}\int\boldsymbol{R}_{\mathrm{s}\epsilon_p}(\hat{\boldsymbol{k}})T_L(k_{\epsilon_q},\hat{\boldsymbol{k}},\boldsymbol{r_{ba}})\boldsymbol{T}_{\mathrm{s}\epsilon_p}(\hat{\boldsymbol{k}})\mathrm{d}^2\hat{\boldsymbol{k}},\end{aligned}\tag{23}$$

where the radiation function is

$$\boldsymbol{T}_{\mathrm{s}\epsilon_p}(\hat{\boldsymbol{k}})=\left(\overline{\overline{I}}-\hat{\boldsymbol{k}}\hat{\boldsymbol{k}}\right)\int_{\boldsymbol{f}_n}\mathrm{e}^{\mathrm{i}k_{\epsilon_p}\hat{\boldsymbol{k}}\hat{\boldsymbol{r}}_{\boldsymbol{r}'\boldsymbol{a}}}\boldsymbol{f}_n(\boldsymbol{r}')\mathrm{d}\boldsymbol{r}',\tag{24}$$

and the receive function is

$$\boldsymbol{R}_{\mathrm{s}\epsilon_p}(\hat{\boldsymbol{k}})=\left(\overline{\overline{I}}-\hat{\boldsymbol{k}}\hat{\boldsymbol{k}}\right)\int_{\boldsymbol{f}_m}\mathrm{e}^{-\mathrm{i}k_{\epsilon_p}\hat{\boldsymbol{k}}\hat{\boldsymbol{r}}_{\boldsymbol{r}\boldsymbol{b}}}\boldsymbol{f}_m(\boldsymbol{r})\mathrm{d}\boldsymbol{r}.\tag{25}$$

2. Applying the addition theorem to Eq. (14), the $\boldsymbol{Z}_{\mathrm{SS}}^{pq}$ element can be written as

$$\begin{aligned}&[\boldsymbol{Z}_{\mathrm{SS}}^{pq}]_{m,n}\\&=-\frac{\mathrm{i}\omega\mu_0}{4\pi}\int\boldsymbol{R}_{\mathrm{s}0}(\hat{\boldsymbol{k}})T_L(k_0,\hat{\boldsymbol{k}},\boldsymbol{r_{ba}})\boldsymbol{T}_{\mathrm{s}0}(\hat{\boldsymbol{k}})\mathrm{d}^2\hat{\boldsymbol{k}},\end{aligned}\tag{26}$$

where the radiation function is

$$\boldsymbol{T}_{\mathrm{s}0}(\hat{\boldsymbol{k}})=\left(\overline{\overline{I}}-\hat{\boldsymbol{k}}\hat{\boldsymbol{k}}\right)\int_{\boldsymbol{f}_n}\mathrm{e}^{\mathrm{i}k_0\hat{\boldsymbol{k}}\hat{\boldsymbol{r}}_{\boldsymbol{r}'\boldsymbol{a}}}\boldsymbol{f}_n(\boldsymbol{r}')\mathrm{d}\boldsymbol{r}',\tag{27}$$

and the receive function is

$$\boldsymbol{R}_{\mathrm{s}0}(\hat{\boldsymbol{k}})=\left(\overline{\overline{I}}-\hat{\boldsymbol{k}}\hat{\boldsymbol{k}}\right)\int_{\boldsymbol{f}_m}\mathrm{e}^{-\mathrm{i}k_0\hat{\boldsymbol{k}}\hat{\boldsymbol{r}}_{\boldsymbol{r}\boldsymbol{b}}}\boldsymbol{f}_m(\boldsymbol{r})\mathrm{d}\boldsymbol{r}.\tag{28}$$

3. Applying the addition theorem to Eq. (17), the $\boldsymbol{Z}_{\mathrm{SV}}$ element can be written as

$$\begin{aligned}&[\boldsymbol{Z}_{\mathrm{SV}}]_{m,n_{\mathrm{t}}}\\&=-\frac{k_0^2(\epsilon-1)}{4\pi}\int\boldsymbol{R}_{\mathrm{s}0}(\hat{\boldsymbol{k}})T_L(k_{\epsilon_q},\hat{\boldsymbol{k}},\boldsymbol{r_{ba}})\\&\cdot\left[T_{\mathrm{v}0}^{x}(\hat{\boldsymbol{k}})\;\;T_{\mathrm{v}0}^{y}(\hat{\boldsymbol{k}})\;\;T_{\mathrm{v}0}^{\mathrm{z}}(\hat{\boldsymbol{k}})\right]^{\mathrm{T}}\mathrm{d}^2\hat{\boldsymbol{k}},\end{aligned}\tag{29}$$

where the radiation function in the volume-to-surface integral process is

$$T_{\mathrm{v}0}^{x,y,z}(\hat{\boldsymbol{k}})=\mathrm{e}^{\mathrm{i}k_0\hat{\boldsymbol{k}}\hat{\boldsymbol{r}}_{\boldsymbol{r}'\boldsymbol{a}}},\tag{30}$$

and the receive function defined on the RWG basis functions on the boundary of the scatterer is the same as Eq. (28).

4. Applying the addition theorem to Eq. (18), the $\boldsymbol{Z}_{\mathrm{VS}}$ element can be written as

$$\begin{aligned}&[\boldsymbol{Z}_{\mathrm{VS}}^{x,y,z}]_{n_{\mathrm{t}},n}\\&=-\frac{\mathrm{i}\omega\mu_0}{4\pi}\int R_{\mathrm{v}\epsilon_p}(\hat{\boldsymbol{k}})T_L(k_{\epsilon_q},\hat{\boldsymbol{k}},\boldsymbol{r_{ba}})\boldsymbol{T}_{\mathrm{s}\epsilon_p}(\hat{\boldsymbol{k}})\mathrm{d}^2\hat{\boldsymbol{k}},\end{aligned}\tag{31}$$

where the element of the radiation function is the same as Eq. (24), and the receive function in tetrahedron's volume is

$$R_{\mathrm{v}\epsilon_p}(\hat{\boldsymbol{k}})=\mathrm{e}^{-\mathrm{i}k_{\epsilon_p}\hat{\boldsymbol{k}}\hat{\boldsymbol{r}}_{\boldsymbol{r}\boldsymbol{b}}}.\tag{32}$$

The addition theorem can accelerate MVM in the iterative solver for matrix equations such as the Jacobi method, Gauss–Seidel method, and conjugate gradient method. The MVM based on the addition theorem has three main steps.

First, the tree-based octree subdivision scheme is used to divide the RWG triangle pairs and tetrahedrons into layered cubes (groups) (Meagher, 1982). In the octree subdivision scheme, the entire object is enclosed in a large cube, which is then partitioned into eight child cubes. Each child cube is then recursively subdivided into eight smaller cubes as long as the edge length of the finest cube is no less than the threshold (0.25λ in this study, where λ is the wavelength). As shown in Fig. 1, a cube (group) can contain only RWG triangle pairs from a single region (group A) or RWG triangle pairs of different sub-regions and tetrahedrons (group B).

Second, for a cube in each layer, other cubes are marked as the near group, the relatively far group, and the far group based on their positions. If cube C_2 adjoins cube C_1, then C_2 is marked as a near group of C_1. If cube C_3 does not adjoin C_1, but their parent cubes are adjoined, then C_3 is marked as a relatively far group of C_1. Other cubes in the same layer are marked as far groups of C_1.

Third, the corresponding near-group impedance elements in the finest layer are computed by conventional MoM and stored explicitly. The MVM related

to the relatively far group in each layer is accelerated by the addition theorem. Thus, the calculations of $\boldsymbol{Z}_{\mathrm{SS}}^{p}$, $\boldsymbol{Z}_{\mathrm{SS}}^{pq}$, $\boldsymbol{Z}_{\mathrm{SV}}$, and $\boldsymbol{Z}_{\mathrm{VS}}$ are accelerated through three processes: upward aggregation, translation, and downward disaggregation (Fig. 1). For each basis function in the finest layer, the aggregated field to the center of its parent group is calculated by the radiation functions, and its disaggregated field is directly calculated by the receive functions. For each cube, the aggregated field to the center of its parent group is aggregated and interpolated, and the disaggregated field is anterpolated and disaggregated from the center of its parent group (Bucci et al., 1991; Chew et al., 2001; Sarvas, 2003). Note that the interpolation and anterpolation are required due to the different sampling rates in different layers when we calculate the integral in Eq. (20).

In the enhanced solution for the strong coupling case, an octree structure with $O(\log N_{\mathrm{s}})$ layers will be constructed. In each layer, the aggregation, translation, and disaggregation processes require $O(N_{\mathrm{v}})$ memory storage and CPU time (Song JM and Chew, 1995). Thus, the enhanced solution in the strong coupling case has $O(N_{\mathrm{s}}^{\alpha}\log N_{\mathrm{s}})$ computational complexity.

4.2 Enhanced solution in the weak coupling case

Considering a composite conductor–dielectric object whose spacing among different homogeneous sub-regions is relatively far (no less than 0.1λ in this study), the coupling among different sub-regions has a weak influence on the final result. Thus, we propose an iterative method to solve GME with weak coupling in this study. The flowchart of the iterative method is illustrated in Fig. 2. There are two main processes: the inner solving process and the iteration process. Details of these two processes will be presented in the following subsections.

4.2.1 Inner solving process

In the inner solving process, the octree structure and the addition theorem are used in each homogeneous region as illustrated in Section 4.1. After the incident field is determined, different homogeneous parts are solved independently. In this implementation, the inner solver of the conductor parts solves

$$\boldsymbol{V}_i^p = \boldsymbol{Z}_{\mathrm{SS}}^{pp}\boldsymbol{I}^p,\ p\in[1,P_{\mathrm{c}}], \tag{33}$$

and the inner solver of the homogeneous dielectric parts solves

$$\boldsymbol{V}_i^p = \boldsymbol{Z}_{\mathrm{SS}}^{p}\boldsymbol{I}^p - \boldsymbol{Z}_{\mathrm{SVS}}^{pp}\boldsymbol{I}^p,\ p\in[P_{\mathrm{c}}+1,P_{\mathrm{c}}+P_{\mathrm{d}}], \tag{34}$$

where $\boldsymbol{V}_i^p$ is the excitation vector of region p in the i^{th} iteration process.

4.2.2 Iteration process

The coupling among different sub-regions is considered in the iteration process. In each iteration

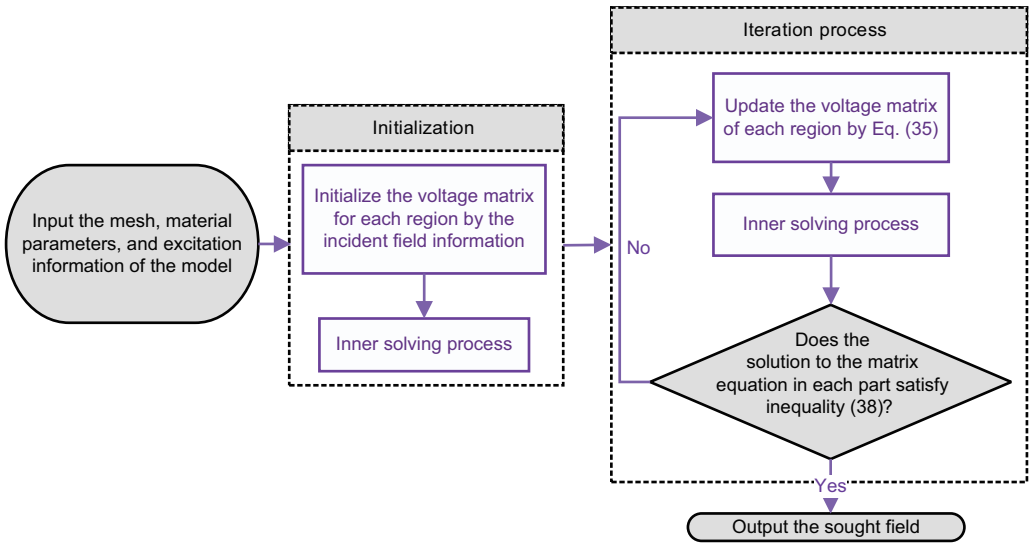

Fig. 2 General flowchart of the enhanced solution in the weak coupling case

process, an additional excitation matrix $\Delta \boldsymbol{V}^p$ is computed for each region, and the excitation matrix of region p in the $(i+1)^{\text{th}}$ iteration is calculated by

$$\boldsymbol{V}_{i+1}^p = \boldsymbol{V}_0^p + \Delta \boldsymbol{V}_{i+1}^p, \tag{35}$$

where

$$\Delta \boldsymbol{V}_{i+1}^p = \begin{cases} \sum\limits_{q=1,q\neq p}^{P_\mathrm{c}} \boldsymbol{Z}_{\mathrm{SS}}^{pq} \boldsymbol{I}_i^q + \sum\limits_{q=P_\mathrm{c}+1}^{P_\mathrm{c}+P_\mathrm{d}} \boldsymbol{Z}_{\mathrm{SVS}}^{pq} \boldsymbol{I}_i^q, \\ \quad p \in [1, P_\mathrm{c}], \\ \sum\limits_{q=1}^{P_\mathrm{c}} \boldsymbol{Z}_{\mathrm{SS}}^{pq} \boldsymbol{I}_i^q + \sum\limits_{q=P_\mathrm{c}+1,q\neq p}^{P_\mathrm{c}+P_\mathrm{d}} \boldsymbol{Z}_{\mathrm{SVS}}^{pq} \boldsymbol{I}_i^q, \\ \quad p \in [P_\mathrm{c}+1, P_\mathrm{c}+P_\mathrm{d}]. \end{cases} \tag{36}$$

In Eq. (36), $\boldsymbol{I}_i^q$ is the current matrix of part q gained in the i^{th} iteration process and $\boldsymbol{V}_0^p$ is the same as $\boldsymbol{V}^p$ in Eq. (16). Due to the weak coupling among different sub-regions, the coupling matrices are of low rank. ACA (Zhao et al., 2005) can be used to compress the coupling matrices. Thus, the low-rank coupling impedance matrices in Eq. (36) can be compressed by

$$\tilde{\boldsymbol{Z}}^{m\times n} \approx \boldsymbol{U}^{m\times r} \boldsymbol{V}^{r\times n}, \tag{37}$$

where r is the effective rank of the $m \times n$ weak coupling matrix $\boldsymbol{Z}$ ($r \ll m, n$), and the $m \times r$ matrix $\boldsymbol{U}$ and $r \times n$ matrix $\boldsymbol{V}$ are dense rectangular matrices.

The iteration process will stop when the current becomes stable, and the stopping criterion is

$$\frac{\|\boldsymbol{I}_p^{i+1} - \boldsymbol{I}_p^i\|}{\|\boldsymbol{I}_p^i\|} < \xi, \tag{38}$$

where $\|\cdot\|$ is the 2-norm form and ξ is the threshold value.

In the enhanced solution in the weak coupling case, the coupling among different sub-regions is accelerated by ACA. The ACA algorithm requires $O(rN_\mathrm{s} + rN_\mathrm{v}) = O(rN_\mathrm{v})$ memory storage and $O(r^2N_\mathrm{s} + r^2N_\mathrm{v}) = O(r^2N_\mathrm{v})$ CPU time (Zhao et al., 2005). After matrix compression, the CPU time for constructing the additional excitation matrices is reduced to $O(rN_\mathrm{v})$. In addition, the computational complexity of the inner solving process is $O(N_\mathrm{s}^\alpha \log N_\mathrm{s})$. Thus, the enhanced solution in the weak coupling case has $O(N_\mathrm{s}^\alpha \log N_\mathrm{s})$ computational complexity.

5 Numerical results

In this section, numerical results are presented to test the efficiency and validity of the proposed method. The following examples are performed on a personal computer with 3.70-GHz Intel® Core™ i7-8700K CPU (six cores are used) and 64 GB RAM. The computational resource requirements of the direct solution to GME and the proposed enhanced solution for all numerical results are presented in Table 1. The number of iteration steps for the strong coupling case in Table 1 is derived from the iterative matrix equation solver, and the number of iteration steps for the weak coupling case is derived from the coupling process between different sub-regions.

As previously mentioned, the enhanced solution can be used to analyze the scattering characteristic of homogeneous objects. For metal objects, let $P_\mathrm{c} = 1$ and $P_\mathrm{d} = 0$ in Eq. (12). For homogeneous dielectric objects, let $P_\mathrm{c} = 0$ and $P_\mathrm{d} = 1$. Here, first, a dielectric almond shape with relative permittivity $(2.0, -0.5)$ is analyzed. The object is discretized by 10 911 tetrahedrons, which leads to 3753 triangle pairs on its surface. The almond is illuminated by a 3.0 GHz vertically polarized incident plane wave from $(\theta, \phi) = (0°, 0°)$. The radar cross section (RCS) in the directions $\theta \in [0°, 360°], \phi = 0°$ is calculated. Fig. 3 shows the RCS results of the enhanced solution and the results of the direct solution and the solution using the FEKO software.

Table 1 Computational resource requirements of the direct and enhanced solutions

Model	N_s	N_v	Time (s)		Decrease in time (%)	Memory (MB)		Decrease in memory (%)	Iteration
			Direct	Enhanced		Direct	Enhanced		
Almond	3753	10 911	839.20	188.40	77.60	6128.70	1106.70	81.94	77
Stratified ball	10 833	31 652	3370.88	352.04	89.60	24 479.00	2705.11	88.90	80
Composite ball	21 915	72 299	45 234.50	1546.30	96.60	64 879.20	6490.33	90.00	138
Discrete object	15 404	74 423	14 008.70	1446.43	89.70	64 021.60	5143.57	92.00	79

N_s: number of triangle pairs; N_v: number of tetrahedrons; Iteration: number of iteration steps in the enhanced solution

Second, two examples are presented to test the accuracy and efficiency of the proposed enhanced solution in the strong coupling case. First, the analysis of a stratified ball is presented. As shown in Fig. 4a, 31 652 tetrahedrons discretize the ball, and 7222 triangles discretize the boundaries of the sub-regions in total, which leads to 10 833 unknowns. The sub-regions formed by dielectric materials A, B, C, D, and the perfect electric conductor (PEC) sub-region contribute 1113, 2307, 3114, 2985, and 1314 unknowns, respectively. The relative error distribution of the total field throughout the dielectric regions with respect to the FEKO solution is presented in Fig. 4b. In addition, the relative error is defined by

$$\mathrm{RE}(\boldsymbol{r}) = \frac{|\boldsymbol{E}^{\mathrm{e}}(\boldsymbol{r}) - \boldsymbol{E}^{\mathrm{FEKO}}(\boldsymbol{r})|}{|\boldsymbol{E}^{\mathrm{FEKO}}(\boldsymbol{r})|}, \tag{39}$$

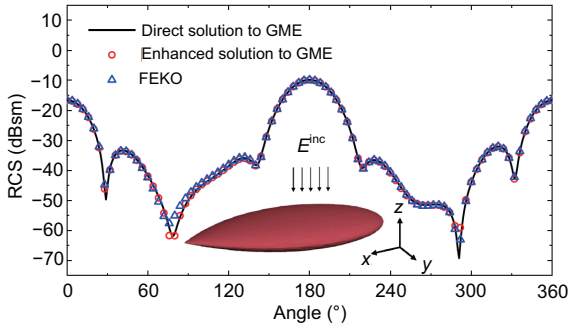

Fig. 3 Bistatic RCS of the almond computed by the direct solution, enhanced solution, and FEKO

where $\mathrm{RE}(\boldsymbol{r})$ is the relative error value at point $\boldsymbol{r}$, $\boldsymbol{E}^{\mathrm{e}}(\boldsymbol{r})$ is the total field calculated by the proposed enhanced solution, and $\boldsymbol{E}^{\mathrm{FEKO}}(\boldsymbol{r})$ is the total field calculated by FEKO, and the norm is defined as the 1-norm form. Then, a composite ball is considered. The composite ball is discretized by 72 299 tetrahedrons, and 14 610 triangles discretize the boundaries of the sub-regions in sum, which leads to 21 915 unknowns. The sub-regions formed by the dielectric materials A, B, C, D, E, and the PEC sub-region contribute 1935, 4086, 4851, 5997, 3972, and 1074 unknowns, respectively, as shown in Fig. 5a. The total field distribution is presented in Fig. 5b. The RCS in directions $\theta \in [0°, 360°], \phi = 0°$ for VV polarization calculated by the enhanced solution is in good agreement with those of the direct solution and the FEKO solution, as shown in Fig. 6.

Third, a discrete object consisting of several discrete sub-regions is analyzed by the proposed enhanced solution in the weak coupling case. As shown in Fig. 7a, the scattering target array is discretized by 74 423 tetrahedrons, and 10 276 triangles discretize the boundaries of the sub-regions in total, which leads to 15 404 unknowns. The inner PEC cube has 608 unknowns, and the dielectric balls (from the ball formed by material A, counterclockwise) have 1119, 1431, 1860, 2253, 2589, 2253, 1860, and 1431 unknowns. The total field distribution is presented in Figs. 7b and 7c. The RCS in directions

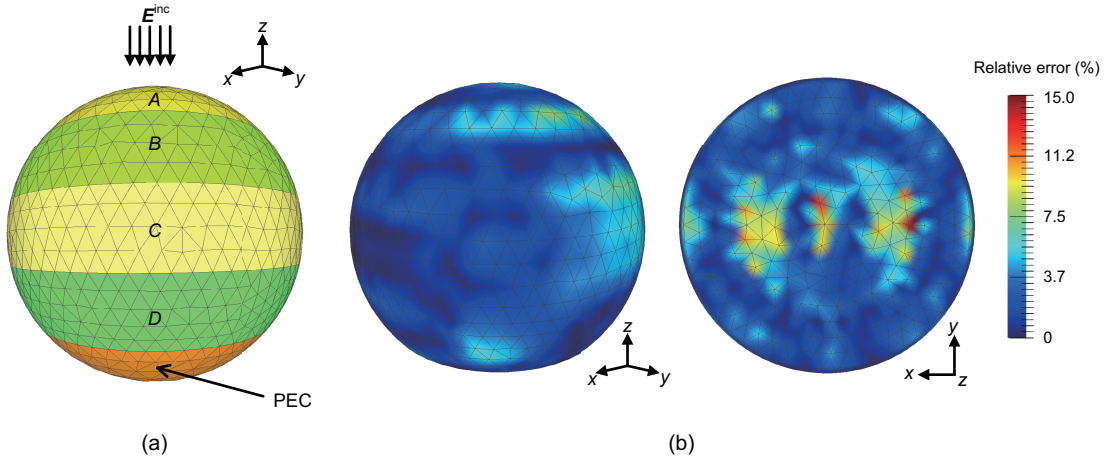

Fig. 4 Model and simulation results of the stratified ball

(a) The ball centered at the origin consists of five sub-regions with the same thickness of 0.04 m. The sub-region at the bottom of the ball is formed by PEC, and the other sub-regions are formed by dielectric materials A, B, C, and D with relative permittivity of 1.5, 2.0, 2.5, and 3.0, respectively. The stratified ball is illuminated by a 1.5 GHz vertically polarized incident wave from $(\theta, \phi) = (0°, 0°)$. (b) The relative error distribution among the dielectric sub-regions of the enhanced solution with respect to the FEKO solution is represented by different colors

$\theta \in [0°, 360°], \phi = 90°$ for VV polarization calculated by the proposed method is in good agreement with those of the direct solution and the FEKO solution, as shown in Fig. 8.

Compared with the direct solution to GME, the proposed enhanced solution generates results with low relative errors, and the proposed method requires only 11.6% memory and 11.8% CPU time on average among these cases. It can be concluded that the enhanced solution has better performance when analyzing homogeneous objects and composite objects compared with the direct solution.

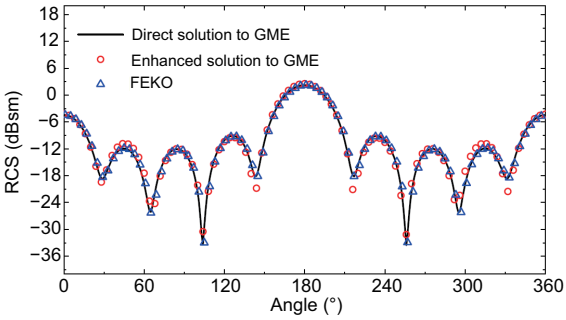

Fig. 6 Bistatic RCS of the composite ball computed by the direct solution, enhanced solution, and FEKO

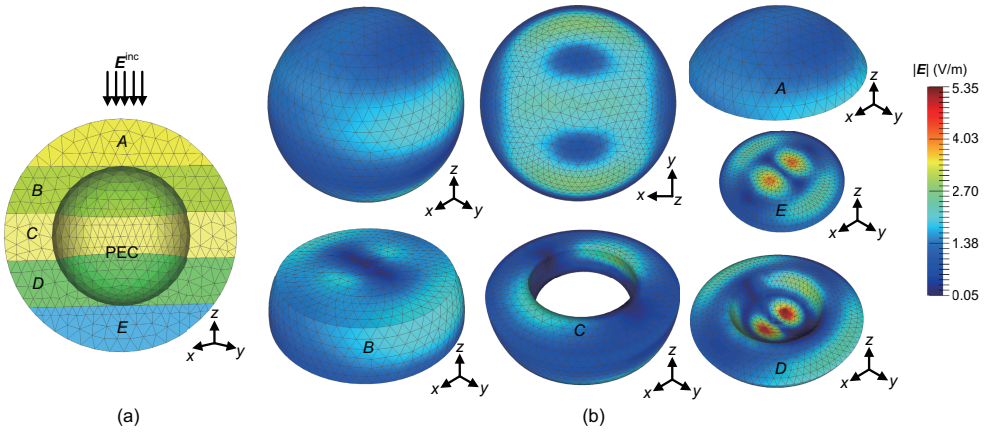

Fig. 5 Model and simulation results of the composite ball

(a) The ball centered at the origin consists of six sub-regions. The inner sphere with a radius of 0.06 m is formed by PEC. The outer layer with a radius of 0.1 m is formed by five dielectric materials A, B, C, D, and E with relative permittivity of 1.5, 2.0, 2.5, 3.0, and 3.5, respectively. The five dielectric sub-regions have the same thickness of 0.04 m. The composite ball is illuminated by a 2.0 GHz vertically polarized incident wave from $(\theta, \phi) = (0°, 0°)$. Note that the concave cut is made for improved visibility. (b) The total field distribution of the object is calculated by the enhanced solution. Different views of the dielectric sub-regions are presented

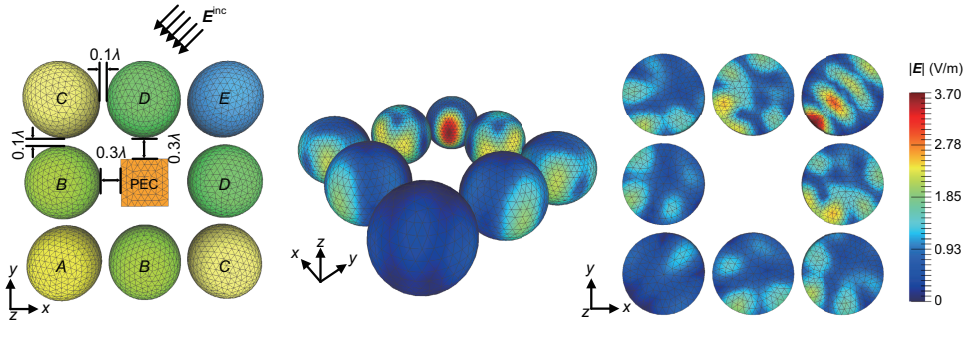

Fig. 7 Model and simulation results of the discrete objects

(a) The discrete objects consist of nine sub-regions. The cube in the center with a side length of 0.06 m is formed by PEC. The eight balls with a radius of 0.05 m around the cube are formed by dielectric materials. The dielectric materials A, B, C, D, and E have relative permittivity of 1.5, 2.0, 2.5, 3.0, and 3.5, respectively. The discrete objects are illuminated by a 3.0 GHz vertically polarized incident wave from $(\theta, \phi) = (90°, 45°)$. (b) The total field distribution among the dielectric sub-regions is calculated by the enhanced solution. (c) The total field distribution among the dielectric regions on the $z = 0$ plane is shown for improved visibility

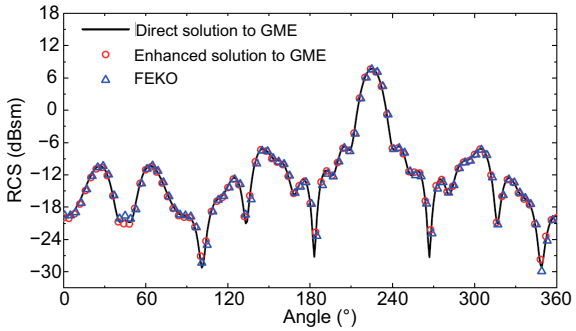

Fig. 8 Bistatic RCS of the discrete object computed by the direct solution, enhanced solution, and FEKO

6 Conclusions

In this paper, an enhanced solution to SVS-EFIE is proposed and implemented to solve the EM scattering problems of metal–dielectric composite objects. Although SVS-EFIE can reduce the number of unknowns when analyzing homogeneous dielectric objects, it can result in complex equations, laborious implementation, and unacceptable computational complexity when it is applied to metal–dielectric composite objects. Thus, GME is first presented to analyze the metal–dielectric composite objects. Note that GME can also be used to analyze the scattering properties of homogeneous objects. Then, the enhanced solution with two policies to GME is proposed. These two policies can be selected adaptively based on the coupling degree concerning the spacing between different subregions. For the strong coupling case, the enhanced solution based on the addition theorem is proposed. For the weak coupling case, the enhanced solution based on the iterative method and algebra-based matrix compression method is proposed. In addition, CPU parallelism can be easily applied to the enhanced solution. Numerical results demonstrate that the proposed method requires only 11.6% memory and 11.8% CPU time on average compared to the previous direct solution. Numerical results demonstrate the efficiency and accuracy of the proposed method.

Contributors

Han WANG designed the research and implemented the code. Mingjie PANG and Hai LIN processed the data. Han WANG drafted the paper. Mingjie PANG helped organize the paper. Han WANG, Mingjie PANG, and Hai LIN revised and finalized the paper.

Compliance with ethics guidelines

Han WANG, Mingjie PANG, and Hai LIN declare that they have no conflict of interest.

References

Bucci OM, Gennarelli C, Savarese C, 1991. Optimal interpolation of radiated fields over a sphere. *IEEE Trans Antenn Propag*, 39(11):1633-1643. https://doi.org/10.1109/8.102779

Chew WC, Jin JM, Michielssen E, et al., 2001. Fast and Efficient Algorithms in Computational Electromagnetics. Artech House, Boston, USA.

Dagum L, Menon R, 1998. OpenMP: an industry standard API for shared-memory programming. *IEEE Comput Sci Eng*, 5(1):46-55. https://doi.org/10.1109/99.660313

Ergul Ö, Gurel L, 2009. Comparison of integral-equation formulations for the fast and accurate solution of scattering problems involving dielectric objects with the multilevel fast multipole algorithm. *IEEE Trans Antenn Propag*, 57(1):176-187. https://doi.org/10.1109/TAP.2008.2009665

Gholami R, Okhmatovski V, 2020. Surface–volume–surface EFIE formulation for fast direct solution of scattering problems on general 3-D composite metal–dielectric objects. *IEEE Trans Antenn Propag*, 68(7):5742-5747. https://doi.org/10.1109/TAP.2020.2968762

Gholami R, Menshov A, Okhmatovski VI, 2019. *H*-matrix accelerated solution of surface–volume–surface EFIE for fast electromagnetic analysis on 3-D composite dielectric objects. *IEEE J Multisc Multiphys Comput Techn*, 4:152-162. https://doi.org/10.1109/JMMCT.2019.2920106

Goni O, Okhmatovski VI, 2021. Analytic solution of surface–volume–surface electric field integral equation on dielectric sphere and analysis of its spectral properties. *IEEE Trans Antenn Propag*, early access. https://doi.org/10.1109/TAP.2021.3083829

Hariharan B, Aluru S, Shanker B, 2002. A scalable parallel fast multipole method for analysis of scattering from perfect electrically conducting surfaces. Proc ACM/IEEE Conf on Supercomputing, Article 42. https://doi.org/10.1109/SC.2002.10012

Lori FSH, Menshov A, Gholami R, et al., 2018. Novel single-source surface integral equation for scattering problems by 3-D dielectric objects. *IEEE Trans Antenn Propag*, 66(2):797-807. https://doi.org/10.1109/TAP.2017.2781740

Lu CC, 2003. A fast algorithm based on volume integral equation for analysis of arbitrarily shaped dielectric radomes. *IEEE Trans Antenn Propag*, 51(3):606-612. https://doi.org/10.1109/TAP.2003.809823

Lu CC, Chew WC, 2000. A coupled surface-volume integral equation approach for the calculation of electromagnetic scattering from composite metallic and material targets. *IEEE Trans Antenn Propag*, 48(12):1866-1868. https://doi.org/10.1109/8.901277

Meagher D, 1982. Geometric modeling using octree encoding. *Comput Graph Image Process*, 19(2):129-147. https://doi.org/10.1016/0146-664X(82)90104-6

Menshov A, Okhmatovski V, 2013. New single-source surface integral equations for scattering on penetrable cylinders and current flow modeling in 2-D conductors. *IEEE Trans Microw Theory Techn*, 61(1):341-350. https://doi.org/10.1109/TMTT.2012.2227784

Poggio AJ, Miller EM, 1973. Integral equation solutions of three-dimensional scattering problems. In: Mittra R (Ed.), Computer Techniques for Electromagnetics: a Volume in International Series of Monographs in Electrical Engineering. Pergamon, New York, USA, p.159-264. https://doi.org/10.1016/B978-0-08-016888-3.50008-8

Rao S, Wilton D, Glisson A, 1982. Electromagnetic scattering by surfaces of arbitrary shape. *IEEE Trans Antenn Propag*, 30(3):409-418. https://doi.org/10.1109/TAP.1982.1142818

Sarvas J, 2003. Performing interpolation and anterpolation entirely by fast Fourier transform in the 3-D multilevel fast multipole algorithm. *SIAM J Numer Anal*, 41(6):2180-2196. https://doi.org/10.1137/S0036142902405655

Song J, Lu CC, Chew WC, 1997. Multilevel fast multipole algorithm for electromagnetic scattering by large complex objects. *IEEE Trans Antenn Propag*, 45(10):1488-1493. https://doi.org/10.1109/8.633855

Song JM, Chew WC, 1995. Multilevel fast-multipole algorithm for solving combined field integral equations of electromagnetic scattering. *Microw Opt Technol Lett*, 10(1):14-19. https://doi.org/10.1002/mop.4650100107

Xie FS, Li WD, 2018. A method of VSIE for electromagnetic scattering by planar composite conductor-dielectric structures. Proc IEEE MTT-S Int Wireless Symp, p.1-4. https://doi.org/10.1109/IEEE-IWS.2018.8400974

Zhao KZ, Vouvakis MN, Lee JF, 2005. The adaptive cross approximation algorithm for accelerated method of moments computations of EMC problems. *IEEE Trans Electromagn Compat*, 47(4):763-773. https://doi.org/10.1109/TEMC.2005.857898

Zheng SC, Gholami R, Okhmatovski VI, 2018. Surface-volume-surface electric field integral equation for solution of scattering problems on 3-D dielectric objects in multilayered media. *IEEE Trans Microw Theory Techn*, 66(12):5399-5414. https://doi.org/10.1109/TMTT.2018.2866855